advantages of this device are its reconfigurable and dynamic filtering features. By including this device in the EDF systems, we demonstrated the flattening of the ASE spectrum and the tunable operation of the fiber laser. We expect that this device can be applied for various fiber components, including tunable filters, variable attenuators, mode converters, and sensors through further investigation.

REFERENCES

1. A.M. Vengsarkar, P.J. Lemaire, J.B. Judkins, V. Bhatia, T. Erdogan, and J.E. Sipe, Long-period fiber gratings as band-rejection filters, J Lightwave Technol 14 (1996), 58–65.
2. S.W. James and R.P. Tatam, Optical fibre long-period grating sensors: Characteristics and application, Meas Sci Technol 14 (2003), R49–R61.
3. Y. Zhu, P. Shum, C. Lu, B.M. Lacquet, P.L. Swart, and S.J. Spammer, EDFA gain flattening using phase-shifted long-period grating, Microwave Opt Technol Lett 37 (2003), 153–157.
4. D.M. Costantini, C.A.P. Muller, S.A. Vasiliev, H.G. Limberger, and R.P. Salathé, Tunable loss filter based on metal-coated long-period fiber grating, IEEE Photon Technol Lett 11 (1999) 1458–1460.
5. S. Savin, M.J.F. Digonnet, G.S. Kino, and H.J. Shaw, Tunable mechanically induced long-period fiber gratings, Opt Lett 25 (2000), 710–712.
6. B.U. Nair, V.P.S. Kumar, V.P.M. Pillai and V.U. Nayar, Wavelength shift of cladding mode resonances in a mechanically induced LPFG by twisting the fiber, Fiber Integr Opt 26 (2007), 159–172.
7. G. Rego, Long-period fiber gratings mechanically induced by winding a string around a fiber/grooved tube set, Microwave Opt Technol Lett 50 (2008), 2064–2068.
8. H. Sakata and K. Yamahata, Magnetic-force-induced long-period fiber gratings, Opt Lett 37 (2012), 1250–1252.
9. H. Sakata, T. Numano, and M. Tomiki, Loss tunable long-period fiber gratings controlled by electromagnet, IEEE Photon Technol Lett 24 (2012) 1680–1682.
10. C.B. Probst, A. Bjarklev, and S.B. Andreasen, Experimental verification of microbending theory using mode coupling to discrete cladding modes, J Lightwave Technol 7 (1989), 55–61.
11. P. Peterka, J. Maria, B. Dussardier, R. Slavík, P. Honzátko, and V. Kubeček, Long-period fiber grating as wavelength selective element in double-clad Yb-doped fiber-ring lasers, Laser Phys Lett 6 (2009), 732–736.

CONTROLLING THE RESONANCES OF INDEFINITE MATERIALS FOR MAXIMIZING EFFICIENCY IN WIRELESS POWER TRANSFER

Yan Zhao and Ekachai Leelarasmee
Faculty of Engineering, Chulalongkorn University, Phayathai Road, Pathumwan, Bangkok 10330, Thailand; *Corresponding author: yan.z@chula.ac.th

ABSTRACT: *In this article, we investigate the possibility of improving efficiency in wireless power transfer (WPT) using metamaterials. Our analysis differs from previous works on the metamaterial design for WPT in that we focus on the design of thin metamaterial slabs. Specifically, three types of metamaterials are considered: the double negative material, the μ-negative material, and the indefinite material (IM). Although in general, all three types of materials are capable of amplifying evanescent waves, when the thickness is small, the slab formed by IM offers the best performance in enhancing WPT efficiency, as the locations of the resonances introduced by the slab can be controlled more readily. Thus, we propose a tuning method by varying its material parameters to maximize the WPT efficiency. Full-wave simulations of a WPT system equipped with a thin IM slab show that the system efficiency can be enhanced by an order of magnitude, comparing with the conventional design. As an example, implementation of the thin IM slab, the capacitively loaded split-ring resonators are considered, and the enhancement of WPT efficiency shows a similar performance to the ideal homogeneous IM slab.* © 2014 Wiley Periodicals, Inc. Microwave Opt Technol Lett 56:867–875, 2014; View this article online at wileyonlinelibrary.com. DOI 10.1002/mop.28212

1. INTRODUCTION

Recently, the development of wireless power transfer (WPT) systems has attracted considerable attention due to the convenience that such technology may bring to our daily lives. Although the original idea was demonstrated more than 100 years ago by Tesla [1], its application has just become more popular in recent years due to the reduction in the energy consumption of electronic devices.

Most existing and commercially available WPT systems are based on inductive coupling, which requires a close proximity between the user device and the charging station, thus it is a major drawback of such systems. For energy transfer over a long distance, the conventional method of microwave power transmission [2] is a viable solution to provide high transfer efficiency, however, the large antenna size (∼1 km diameter) and the large amount of transmitted power prohibit their consumer applications and may cause hazardous health effect to human beings. In 2007, a more efficient WPT scheme of resonant coupling was proposed and experimentally demonstrated [3]. Since then, much work has been done to improve the efficiency of WPT systems [4].

In inductive coupling-based WPT systems, evanescent waves play a key role. However, as they decay exponentially in free-space, when the distance between the source and end devices increases, the efficiency of such systems decreases rapidly. Researchers have attempted to seek novel materials or structures that can enhance evanescent waves and improve the WPT efficiency. One type of the potential candidates, the so-called metamaterials, which are artificial structures with extraordinary and desirable electromagnetic properties [5], have been applied for evanescent wave amplification [6, 7], and to improve the efficiency of WPT systems [8–11]. In these works, although both isotropic and anisotropic metamaterials have been considered, either the relative permeability of equal to or less than −1 is always assumed [8–10], or the thickness of the metamaterial slab placed between the transmitting and receiving antennas is large comparing with the distance, to satisfy the "perfect lens" condition [11].

In our present work, with the consideration of practical implementation in mind, we focus on the design of a thin metamaterial slab (typically less than 20% of the transmitter–receiver distance), and investigate the possibility of maximizing the efficiency of WPT systems. We first analyze the behavior of evanescent waves inside different types of metamaterials and then show that the locations of the resonances introduced by indefinite materials (IMs) [12] are sensitive to material properties and can be controlled to enhance evanescent waves with different wave numbers. Tuning material parameters to control the
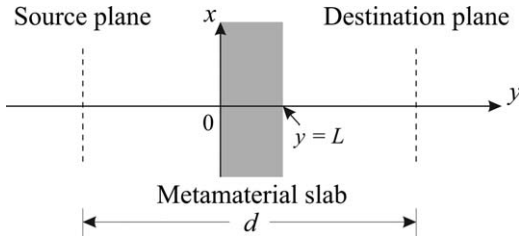
Figure 1 System configuration for the analysis of plane-wave transmission through metamaterial slabs

transmission spectrum have also been investigated in [13] to achieve subwavelength imaging [14]. Our goal is to maximize evanescent wave amplification for a wide range of low-order wave numbers, to greatly enhance the WPT efficiency.

2. AMPLIFICATION OF EVANESCENT WAVES BY METAMATERIAL SLABS

In this work, three types of metamaterials are considered: the double negative material (DNG, $\varepsilon = \mu = -1$) [15], the isotropic μ-negative material (MNG, $\varepsilon = 1$, $\mu < 0$) [5], and IM ($\varepsilon \geq 1, \mu_x = 1$, $\mu_y < 0$, see Fig. 1) [12]. Before applying these materials to WPT systems, it is necessary to investigate how plane-waves are affected, when transmitted through them. Figure 1 shows the system configuration for the calculation of transmission coefficients for slabs formed by different types of metamaterials. The slab is infinite in both x- and z-directions, and its planar boundaries are perpendicular to y-direction. As we are mainly concerned with how the magnetic field component is affected by the metamaterial, the original problem can be reduced to the two-dimensional (2D) transverse electric (TE) case (with respect to the material interface). Hence, only three field components are nonzero: H_x, H_y, and E_z. In different regions, the tangential electric and magnetic field components, E_z and H_x can be expressed as

$$E_z = E_0 e^{-jk_x x} \begin{cases} e^{-jk_y y} + R e^{jk_y y}, & y < 0, \\ A e^{-jq_y y} + B e^{jq_y y}, & 0 \leq y \leq L, \\ T e^{-jk_y(y-L)}, & y > L, \end{cases} \quad (1)$$

$$H_x = \frac{E_0}{\omega \mu_x} e^{-jk_x x} \begin{cases} k_y(e^{-jk_y y} - R e^{jk_y y}), & y < 0, \\ q_y(A e^{-jq_y y} - B e^{jq_y y}), & 0 \leq y \leq L, \\ k_y T e^{-jk_y(y-L)}, & y > L, \end{cases} \quad (2)$$

where E_0 is the magnitude of the incidence wave, k_x and k_y are wave numbers along x- and y-directions in free-space, respectively ($k_x^2 + k_y^2 = k_0^2$, where k_0 is the free-space wave number), q_y is the wave number along y-direction inside the metamaterial slab, R and T are reflection and transmission coefficients, and A and B are the amplitudes of waves inside the metamaterial traveling in forward and backward directions, respectively. By matching boundary conditions at $y = 0$ and $y = L$ such that the tangential field components (1) and (2) are continuous, the transmission coefficient can be calculated as

$$T = \frac{2q_y k_y}{(q_y + k_y)^2 e^{-jq_y L} - (q_y - k_y)^2 e^{jq_y L}}. \quad (3)$$

Note that the above transmission coefficient is calculated from the front to the back interface of the metamaterial slab.

Thus, the total transmission coefficient from the source to the destination planes taking into account wave propagation (decay for evanescent wave components) in the free-space region is given by

$$T' = \frac{2q_y k_y e^{-jk_y(d-L)}}{(q_y + k_y)^2 e^{-jq_y L} - (q_y - k_y)^2 e^{jq_y L}}. \quad (4)$$

For DNG ($\varepsilon = \mu = -1$) and MNG ($\varepsilon = 1$, $\mu < 0$), q_y can be calculated as

$$q_y = \sqrt{\varepsilon \mu k_0^2 - k_x^2}, \quad (5)$$

For IM ($\varepsilon \geq 1$, $\mu_x = 1$, $\mu_y < 0$), q_y is given by

$$q_y = \sqrt{\varepsilon k_0^2 - \frac{k_x^2}{\mu_y}}. \quad (6)$$

It is well known that surface plasmon-like modes can be excited at the interface between media with positive and negative material parameters. For a layered structure with negative material parameters embedded in a medium with positive material parameters, strong resonant modes can be supported [16]. The resonant conditions for such modes are given by the solutions to the following equation:

$$(q_y + k_y)^2 e^{-jq_y L} = (q_y - k_y)^2 e^{jq_y L}, \quad (7)$$

that is, when the denominator of Eq. (3) equals zero. Equation (7) cannot be solved by any direct means, but its solutions may be expressible using the so-called Lambert W function [17], or approximated using the Newton's method. Alternatively, in the current work, we evaluate the transmission coefficients given by Eqs. (3) and (4) with varying transverse wave numbers k_x, to analyze whether resonances exist for different types of metamaterials, and how they are affected by material parameters.

First, we investigate how evanescent waves are affected by relatively thick metamaterial slabs. The distance between the source and destination planes is $d = 1$ m, and the thickness of the slab is $L = 0.4$ m, as shown in Figure 1. In the calculations, a small amount of loss ($\tan \delta = 0.01$) for negative material parameters is also introduced to characterize realistic metamaterials. Figure 2 shows the calculated transmission coefficient (4) for the above three types of metamaterials with varying material parameters, as well as for the free-space case when no metamaterial slabs are present. For the DNG case, as the thickness is approaching the perfect lens condition, the wave components with $k_x > k_0$ are amplified, due to the resonant excitation of surface plasmons at the interfaces of the DNG slab [16].

The amplification of evanescent waves also occurs for MNG and IM, however, in their transmission spectra there exist additional resonances. In particular, two resonances have been found for MNG corresponding to the two resonant modes [16]. For IM, an infinite number of periodically located resonances (except the fundamental one) can be identified. These resonances result in the transmission coefficients exceeding the unity at low-order wave numbers. The locations of the resonances are sensitive to material parameters, as demonstrated in Figure 2, which can be tuned closer so that evanescent waves with a wide range of transverse wave numbers can be amplified. As for the purpose of WPT, evanescent waves with smaller wave numbers are of major concern [13]. Thus, the tuning of the second resonance to merge with the first one is essential for improving the
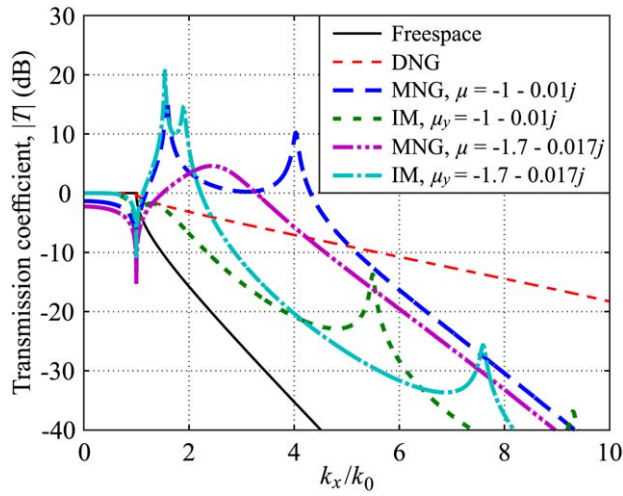
Figure 2 Comparison of transmission coefficient for slabs formed by DNG, MNG, and IM. The distance between the source and destination planes is $d = 1$ m, and the thickness of the slabs is $L=0.4$ m. [Color figure can be viewed in the online issue, which is available at wileyonlinelibrary.com]

efficiency of WPT. Nonetheless, the location dependency of the second resonance on the material parameters is different for MNG and IM, that is, when the relative permeability value is reduced, the second resonance for MNG shifts toward the smaller wave numbers, whereas the one for IM moves in the opposite direction. From the comparison in Figure 2, it is clear that MNG may offer greater enhancement in WPT efficiency than DNG and IM, when the thickness of the slab is large and the negative material parameters are close to -1.

We now turn our attention to thin metamaterial slabs. Figure 3 shows the calculated transmission coefficient for $L=0.2$ m, and all other parameters remain unchanged. As the thickness of the slab is reduced, the amplification of evanescent waves by DNG degrades considerably; whereas for both MNG and IM, their second resonances shift to larger wave numbers. Similar to the previous case, increasing μ_y for IM can shift the second resonance back to merge with the first one. However, for MNG, reducing μ not only lowers the second resonance but also causes the first resonance to move to a larger wave number. Thus these two resonances can only meet at a very large wave number at which the evanescent wave decays too fast to contribute to WPT. Conversely, reducing μ to a moderate value may slightly improve the performance, as illustrated in Figure 3. This allows us to conclude that for thin metamaterial slabs, IMs can be a potential candidate and easily tuned to enhance the amplification of evanescent waves. In the following analysis, we concentrate on IM and investigate its ability to enhance efficiency in WPT.

3. TUNING IMs FOR EVANESCENT WAVE AMPLIFICATION

To further demonstrate how the locations of resonances are affected by material parameters, Eq. (3) is analyzed with varying μ_y and L. Figure 4 shows normalized distributions of resonances represented by bright colors. It can be seen that the first two resonances can be brought closer when L is fixed and μ_y is increased or when μ_y is fixed and L is increased. Thus, there exist different combinations of μ_y and L that a wide range of evanescent waves can be significantly amplified. It is, therefore, necessary to define a figure of merit that can quantify the performance of IM in efficiency enhancement for WPT. The mutual inductance enhancement factor defined in [11] is a good

measure and used in our analysis to compare with numerical simulation results in Section 4:

$$\rho = \frac{L_{21}}{L_{21}^{\text{vac}}}, \qquad (8)$$

where L_{21} is the mutual inductance between two small loop antennas in the presence of an IM, as defined in [10]:

$$L_{21} = \frac{\mu_0 \pi R^4}{2} \frac{4\alpha/\mu_x}{a(2\alpha L)^3} \Phi_L\left(-b/a, 3, \frac{\alpha L + d - L}{2\alpha L}\right), \qquad (9)$$

and μ_0 is the free-space permeability, μ_x and μ_y are effective permeabilities of IM in x- and y-directions, respectively, R is the radius of the small loop antennas, $\alpha = \sqrt{\mu_x/\mu_y}$, $a = -(\alpha/\mu_x + 1)^2$, $b = (\alpha/\mu_x - 1)^2$, and Φ_L is the standard Lerch transcendent function [18]. The mutual inductance between two small loop antennas in free-space can then be calculated as:

$$L_{21}^{\text{vac}} = -\frac{\mu_0 \pi R^4}{2d^3}. \qquad (10)$$

In addition to Eq. (8), numerical simulations using the finite-difference time-domain (FDTD) method [19] are also performed to verify the enhancement of magnetic field due to the introduction of IM. The system shown in Figure 1 can be modeled using 2-D FDTD simulations with TE polarization (only H_x, H_y, and E_z are nonzero). The IM slab is modeled as a homogeneous material with its associated dielectric and magnetic properties. As the relative permeability of the slab is negative, it cannot be directly implemented in conventional FDTD simulations, thus the Drude dispersion model [20] is used to characterize the material property:

$$\mu_y(\omega) = 1 - \frac{\omega_p^2}{\omega^2 - j\omega\gamma}, \qquad (11)$$

where ω_p and γ are the plasma and collision frequencies of the material, respectively. A desired value of μ_y, ω_p, and γ can be
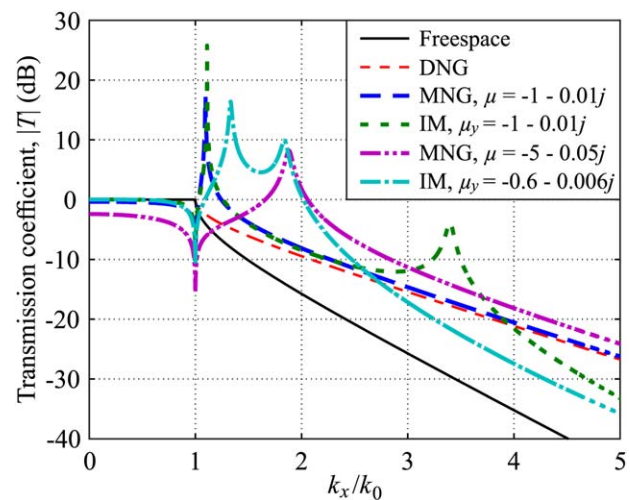

Figure 3 Comparison of transmission coefficient for slabs formed by DNG, MNG, and IM. The distance between the source and destination planes is $d = 1$ m, and the thickness of the slabs is $L=0.2$ m. [Color figure can be viewed in the online issue, which is available at wileyonlinelibrary.com]
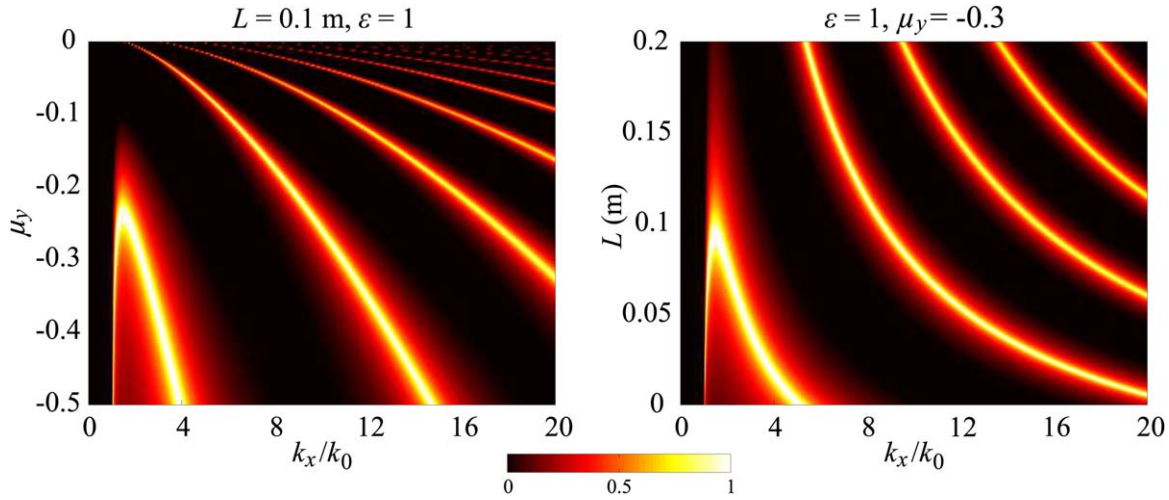
Figure 4 Locations of resonances introduced by thin IM slabs with varying relative permeability along the anisotropy axis (left), and varying thickness of the slab (right). [Color figure can be viewed in the online issue, which is available at wileyonlinelibrary.com]

calculated and used in the dispersive FDTD method [21]. Due to the negative value of μ_y, it is also necessary to apply averaging of material parameters at the boundary of the IM slab, to guarantee accurate FDTD simulations [22]. The FDTD cell size is chosen to be 5×10^{-3} m.

For the source excitation, rather than modeling the curved metallic part of a small loop antenna, which requires a very fine spatial discretization, a magnetic dipole source is defined instead, which is implemented by exciting the H_y component at a single FDTD cell on the symmetry axis of the IM slab. In all FDTD simulations, the distance between the source and destination planes is kept fixed, that is, $d = 1$ m, and the IM slab is located at equal distances from both the source and destination planes. The magnetic field component H_y at the destination point (a single FDTD cell on the symmetry axis of the slab) is then recorded for the two cases of with and without the presence of the IM slab, when the steady-state is reached in simulations. Then the field enhancement factor is calculated as:

$$\tilde{\rho} = \frac{H_y^s}{H_y^0}, \tag{12}$$

where H_y^s is the recorded magnetic field in the presence of the IM slab, and H_y^0 is the calculated magnetic field in free-space.

In all former analyses, the transverse dimension of the IM slab is always infinite. To model infinite structures in FDTD simulations, period boundary conditions (PBCs) can be applied [19]. However, PBCs also cause the magnetic dipole source to be repeated infinitely, which may introduce ambiguity in our analysis and prolong the convergence time in simulations. Conversely, it is found in [11] that when the transverse length of the IM slab is larger than one wavelength of the source excitation, numerical results show good agreement with analytical ones. Thus, in our FDTD simulations, we apply perfectly matched layers (PMLs) boundary conditions [23], and first model an IM slab with its transverse dimension of $w = 1.2 \lambda$, where $\lambda = 3$ m is the free-space wavelength at 100 MHz. Although in previous works by other researchers much lower frequencies are considered, from the practical implementation point of view, reasonable-sized magnetic loop antennas with their diameter of less than half a meter operating at frequencies up to a few tens of MHz usually have very poor efficiency. Thus, the overall efficiency of the WPT system is limited by the efficiency of the antenna itself. At higher frequencies around 100 MHz, the efficiency of the loop antenna with a reasonable size can reach nearly 100%. Besides, the designed WPT system operating at 100 MHz can find its applications in powering
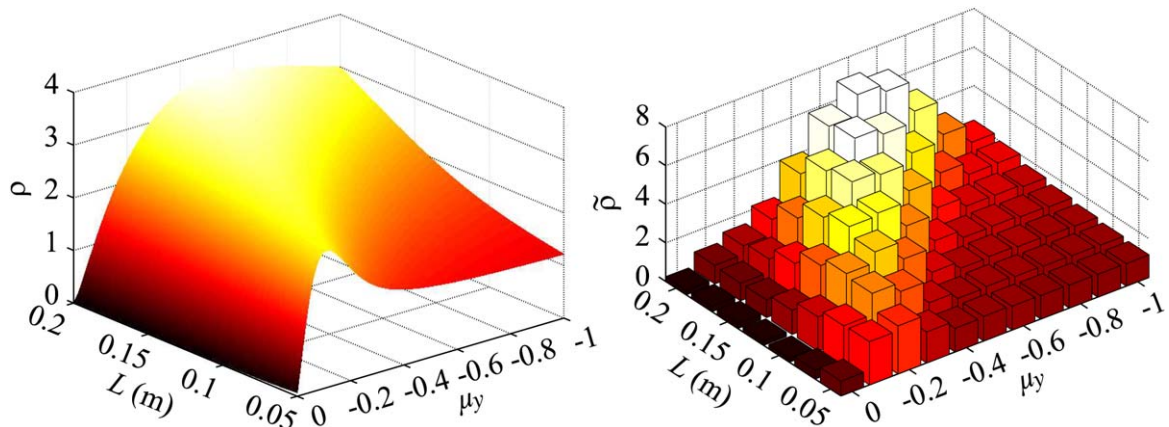

Figure 5 Comparison between the theoretical mutual inductance enhancement factor ρ (left) and the field enhancement factor $\tilde{\rho}$ calculated from FDTD simulations (right), for IM slabs with varying slab thickness L and relative permeability μ_y. Each vertical bar represents a single FDTD run. [Color figure can be viewed in the online issue, which is available at wileyonlinelibrary.com]
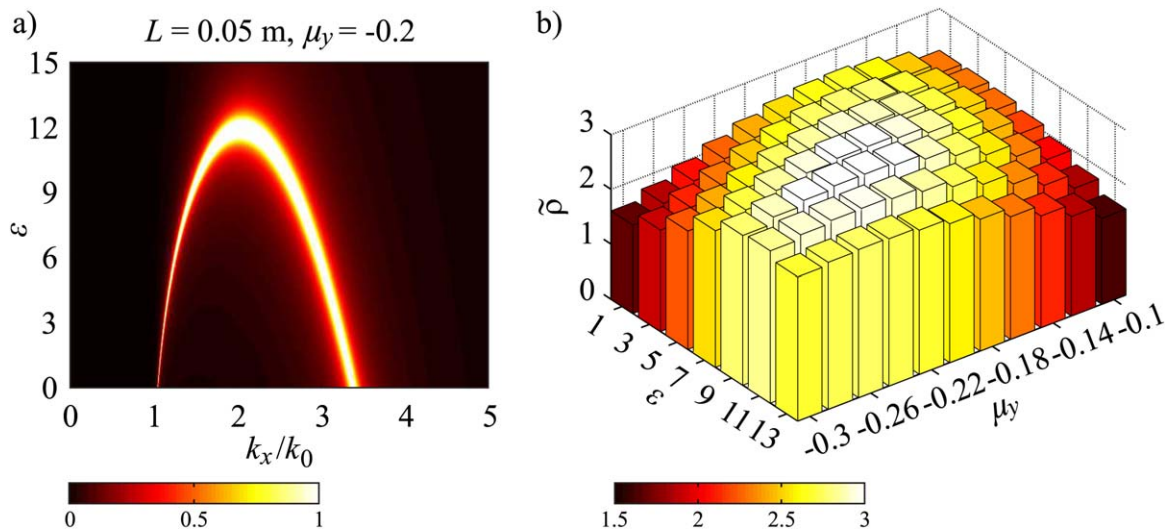
Figure 6 (a) Locations of the first two resonances introduced by IM slabs with varying dielectric constant ε. (b) The field enhancement factor $\tilde{\rho}$ with varying dielectric constant ε and relative permeability μ_y calculated from FDTD simulations. [Color figure can be viewed in the online issue, which is available at wileyonlinelibrary.com]

neural implants in which the on-chip power receiver operates at the same frequency [24].

Figure 5 shows the comparison between the mutual inductance enhancement factor ρ given by Eq. (8) and the field enhancement factor $\tilde{\rho}$ calculated from FDTD simulations, for different combinations of the slab thickness L and relative permeability μ_y. In general, the comparison in Figure 5 shows the same behavior for $\tilde{\rho}$ and ρ: when the thickness of the slab increases, not only the locations of the maximum value of enhancement factors move toward lower permeability values but also the width of the curve is broadened. This allows a higher tolerance in the practical realization of IM such that the permeability value of the fabricated device may deviate from that of the theoretical design. As IMs must be intrinsically dispersive, a wider range of permeability values that can provide good enhancement of mutual inductance also means the device with larger thickness has a wider operational bandwidth.

In the theoretical calculation of ρ, as the contribution from transverse magnetic waves to the total enhancement of mutual

inductance is neglected, Eq. (9) does not predict the mutual inductance when the IM slab has dielectric properties. In our FDTD simulations, we allow the dielectric constant of the slab to vary, and investigate its effect on the enhancement of evanescent waves. As we are mainly interested in the design of compact WPT systems, the thickness of the IM slab is chosen to be $L=0.05$ m. Figure 6(a) shows the location map of the first two resonances calculated using Eq. (3), with varying dielectric constant and $\mu_y = -0.2$ being fixed. It is clear that the second resonance shifts toward the smaller wave numbers when the dielectric constant is increased. Thus, we can predict that when $\varepsilon \approx 9$, $\tilde{\rho}$ can be further increased comparing with the case for $\varepsilon = 1$, which is verified by FDTD simulation results shown in Figure 6(b). Furthermore, not only the value of $\tilde{\rho}$ is higher but also the peak location slightly shifts toward the lower permeability values. These results provide useful indications for the practical implementation of the system, in which negative permeability can be achieved using split-ring resonators (SRRs) [25]. When the relative permeability of the fabricated structure is lower than the design value, dielectric materials can be placed between layers of the SRR structure for fine system tuning.
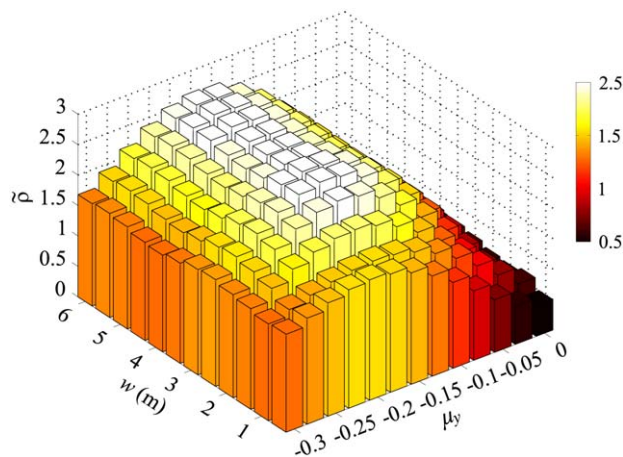

Figure 7 The field enhancement factor $\tilde{\rho}$ with varying transverse dimension w and relative permeability μ_y of the IM slab calculated from FDTD simulations. [Color figure can be viewed in the online issue, which is available at wileyonlinelibrary.com]
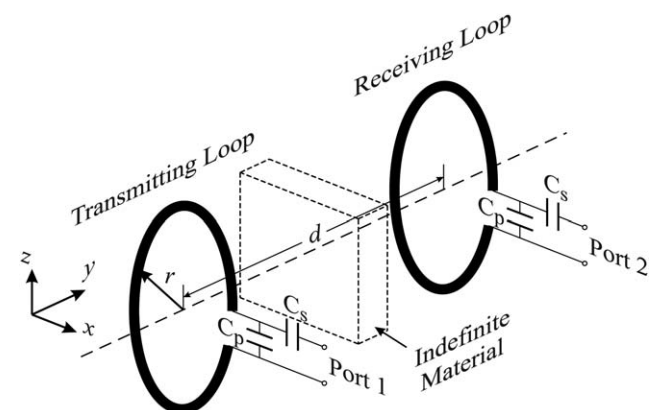

Figure 8 Simulation setup for a WPT system containing two loop antennas. A simple tuning circuit consisting of two capacitors is also included to match the impedance of the loop antennas to 50 Ω
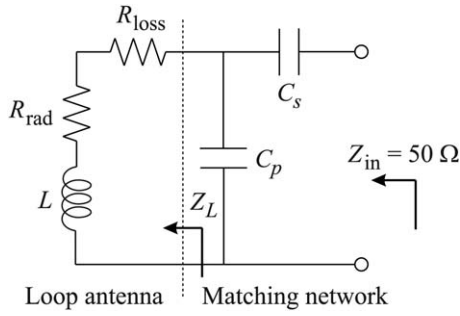
Figure 9 Equivalent circuit and a simple matching network for a small loop antenna

One advantage of applying FDTD simulations is that structures with finite transverse dimensions can be modeled. In our analysis, the transverse dimension of the IM slab is varied to analyze the finite-size effect on the enhancement of magnetic field. Figure 7 shows the FDTD simulation results for $w=0.5$ m ($\lambda/6$) to $w=6$ m (2λ). As the transverse dimension of the slab increases, the value of $\tilde{\rho}$ increases accordingly, and becomes stabilized when $w > \lambda$, in agreement with [11]. In addition, when the transverse dimension is small, the peak location also shifts slightly. The results indicate that the transverse dimension should be large enough to provide high enhancement of evanescent waves.

4. EFFICIENCY ENHANCEMENT FOR WPT SYSTEMS USING IMs

The previous results show that the value of the field enhancement factor $\tilde{\rho} \approx 3$ can be achieved. This means that one can expect up to an order of magnitude enhancement in efficiency for a WPT system equipped with an IM slab. In our analysis, we perform three-dimensional (3D) FDTD simulations to model a WPT system consisting of two circular loop antennas, as shown in Figure 8. The operating frequency of the loop antennas is 100 MHz. For practical considerations, to match the loop antennas to 50 Ω, a matching network containing two capacitors is also designed. Figure 9 shows the equivalent circuit of the loop antenna and the matching network. The capacitance values of C_s and C_p can be calculated through the following steps. First the impedance of the loop antenna can be calculated as

$$Z_L = R_L + jX_L = (R_{rad} + R_{loss}) + jX_L, \qquad (13)$$

where R_{rad} is the radiation resistance, R_{loss} is the loss resistance, and X_L is the inductive reactance of the loop. The capacitors C_s and C_p are used to tune the impedance of the loop antenna, Z_{in}, which can be calculated as

$$Z_{in} = R_{in} + jX_{in} = -jX_s + \frac{1}{\frac{j}{X_p} + \frac{1}{R_L + jX_L}}. \qquad (14)$$

After simple manipulations, to match Z_{in} to 50 Ω, the following expressions for the real and imaginary parts of Z_{in} should be satisfied:

$$R_{in} = \frac{X_p^2 R_L}{(X_p - X_L)^2 + R_L^2} = 50, \qquad (15)$$

$$X_{in} = \frac{X_L X_p^2 - X_L^2 X_p - X_p R_L^2}{(X_p - X_L)^2 + R_L^2} - X_s = 0. \qquad (16)$$

In our design, the radius of the loop antennas is $r = 15$ cm, and the diameter of the wire is 1.6 cm. The loop antennas are

assumed to be copper with conductivity $\sigma = 5.8 \times 10^7$ S/m. Then the values of R_L and X_L can be estimated as: $R_L = 2.0$ Ω, $X_L = 355.6$ Ω [26], and the values of X_s and X_p are calculated as: $X_p = 444.6$ Ω and $X_s = 1775.7$ Ω, corresponding to $C_p = 3.6$ pF and $C_s = 0.9$ pF. These capacitance values are then modeled in FDTD simulations following the approach given in [27]. However, from FDTD simulations, it is found that these theoretically calculated values cause the loop antennas to resonate at around 90 MHz, due to the difference in their actual impedance and the theoretical value [19]. To shift the resonance back to 100 MHz, the capacitance values are found to be $C_p = 1.51$ pF and $C_s = 0.9$ pF.

The FDTD simulation domain is represented by a 3D Cartesian grid with periods Δx, Δy, and Δz along the x-, y-, and z-directions, respectively. The FDTD cell size is chosen to be the same in all directions, that is, $\Delta x = \Delta y = \Delta z = 0.002$ m, equivalent to a spatial resolution of $\lambda/1500$ at 100 MHz. The modeled space has dimensions of $1.8 \times 1.8 \times 2.5$ m^3, which require a large amount of computer memory, and the parallel FDTD method is applied [21]. The outer boundary of the FDTD domain is truncated by a 20-layer PML [23]. The thickness of the IM slab is fixed as $L = 0.05$ m, while its transverse dimension w is varied in simulations, that is, $w = 0.5$ m and $w = 4$ m. The IM slab is located at equal distances from both loop antennas. The
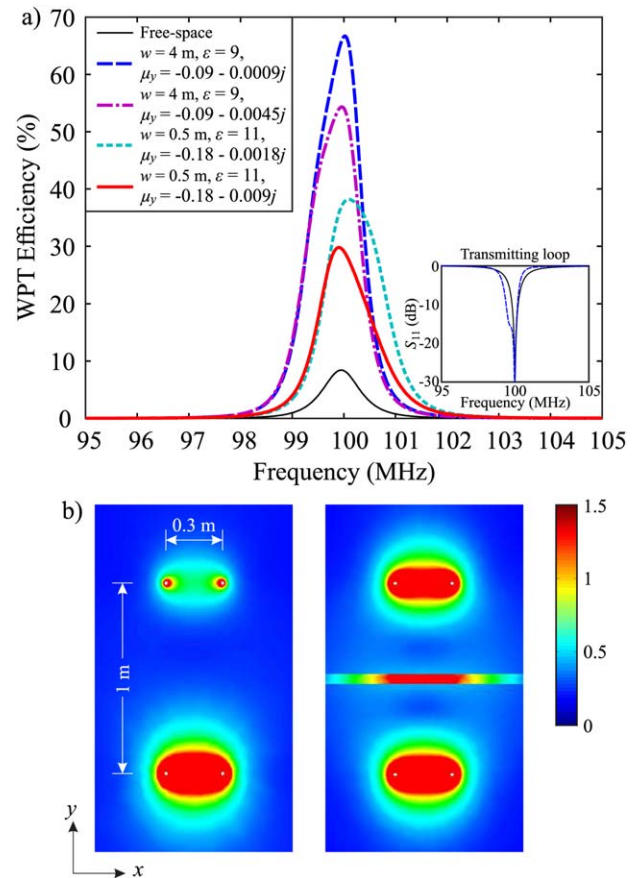

Figure 10 (a) Comparison of system efficiency for IM-enhanced WPT systems with varying slab transverse dimension w and material loss $\tan \delta$. Inset: Return loss (S_{11}) of the transmitting loop antenna. (b) Amplitude of the total magnetic field distributions for a conventional WPT system (left) and an IM-enhanced WPT system with $w = 4$ m and $\tan \delta = 0.01$ (right) at 100 MHz. Only the central part of the simulation domain is shown. [Color figure can be viewed in the online issue, which is available at wileyonlinelibrary.com]
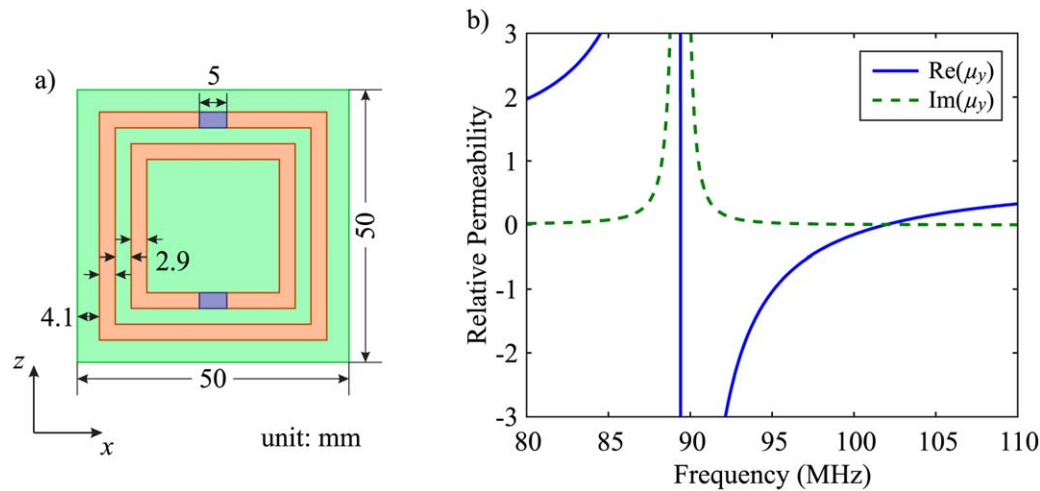
Figure 11 (a) Unit cell of the CLSRR structure. Two 33 pF capacitors are placed at the gaps of split rings. (b) Extracted effective relative permeability for the CLSRR structure. The real and imaginary parts of the relative permeability at 100 MHz are approximately −0.15 and 0.006, respectively, corresponding to tan δ=0.04. [Color figure can be viewed in the online issue, which is available at wileyonlinelibrary.com]

transmitting loop antenna is excited using the delta-gap excitation [19] by a wide-band Gaussian pulse centered at 100 MHz and covering the frequencies of interest at 80–120 MHz. The received electric field component E_z at the location of Port 2 is converted to voltage for the calculation of the scattering parameters S_{11} and S_{21}. Then the efficiency of the WPT system is calculated as $|S_{21}|^2/(1-|S_{11}|^2)$ [4].

Figure 10 shows the comparison of WPT efficiency with and without the presence of the IM slab. From the magnetic field distributions, it is apparent that with the use of IM slab, much higher energy is coupled to the receiving loop antenna. In terms of the system efficiency, it is approximately 7% for the free-space case, in agreement with the theoretical prediction [4]. For the system with the IM slab, the relative permeability and

dielectric constant have been varied to find the optimum system efficiency for each case. In addition, due to the mutual inductance introduced by the IM slab, the impedance of the loop antennas is affected, and the peak efficiency shifts to a higher frequency. Thus, the capacitances in the matching network are varied to shift the frequency back to 100 MHz, and it is found that C_p=1.57 pF and C_p=1.53 pF for $w=4$ m and w=0.5 m, respectively. Figure 10(a) demonstrates that when the loss of the slab is small and its transverse dimension is large, we can achieve nearly an order of magnitude enhancement in efficiency of about 67%. However, the increased loss considerably degrades such an enhancement and the efficiency decreases to about 54% for tan δ=0.05. The reduction in the transverse dimension of the slab further degrades the system performance,
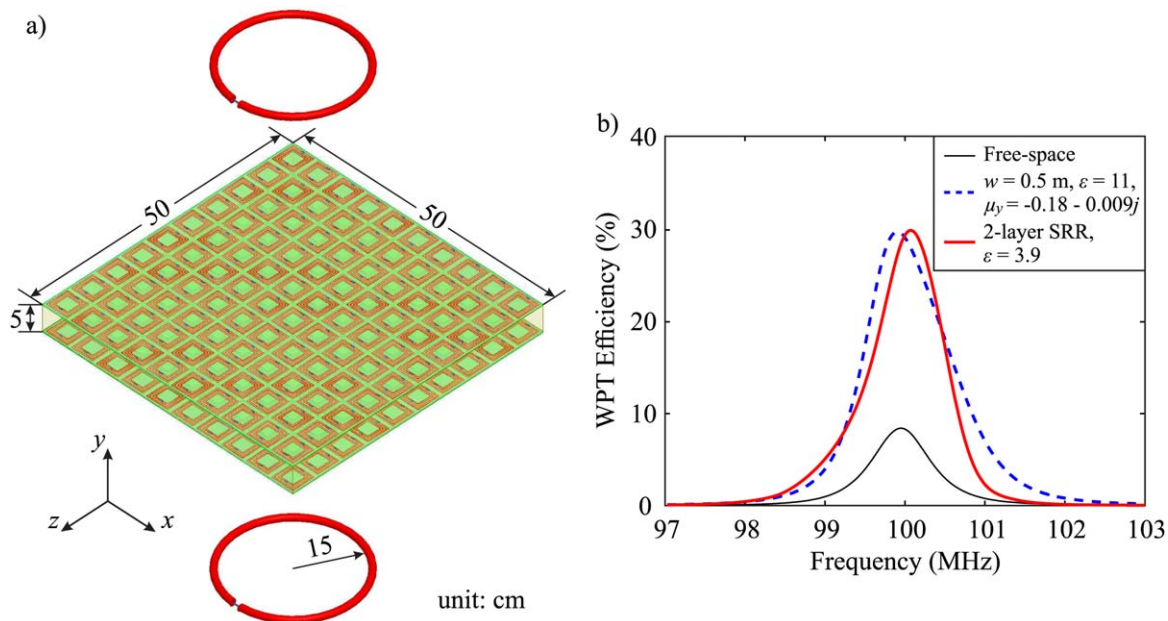

Figure 12 (a) Configuration of the proposed IM-enhanced WPT system consisting of two loop antennas and an IM slab implemented using a two-layer CLSRR structure. A dielectric material with ε=3.9 is placed between the SRR layers. (b) Comparison of system efficiency for the conventional WPT system (free-space), and the IM-enhanced WPT systems with a homogeneous IM slab and the IM slab formed by the CLSRR structure. [Color figure can be viewed in the online issue, which is available at wileyonlinelibrary.com]

and one can only achieve less than 30% efficiency for a slab with $w=0.5$ m and $\tan\delta=0.05$. This allows us to conclude that for high enhancement of WPT efficiency using IMs, the transverse dimension of the slab should be sufficiently large, and the loss in the material should be as small as possible.

Finally, as an example implementation of the IM slab, we consider a capacitively loaded SRR (CLSRR) structure. The unit cell of the structure is shown in Figure 11(a). The capacitors are included in the design for the purpose of reducing the overall size of the CLSRR structure, such that a small thickness of the IM slab can be achieved. The capacitance value is 33 pF and the width of the CLSRR unit cell is 5 cm. At 100 MHz, the period of the CLSRR structure is equal to $\lambda/60$, thus according to the effective medium theory, the structure can be considered as homogeneous. We then follow the method introduced in [28] and perform plane-wave analysis using the 3D FDTD method, to calculate transmission and reflection coefficients and retrieve the effective permeability of the CLSRR structure. During the analysis, only a single layer of the CLSRR structure is considered and the gap size between the conductors, and the distance between the outer conductor and the edge of the unit cell are varied to achieve the desired material parameters according to Figure 10. As shown in Figure 11(b), the real and imaginary parts of the extracted relative permeability at 100 MHz are approximately -0.15 and 0.006, respectively, corresponding to the material loss of $\tan\delta=0.04$.

To construct a thin and finite-sized IM slab, we consider a two-layer CLSRR structure containing 10×10 elements in each layer, as shown in Figure 12(a). The overall dimension of the CLSRR slab is $0.5\times0.5\times0.05$ m^3, same as one of the homogeneous IM slabs considered earlier. Due to the highly intensive computation of the WPT system with the proposed CLSRR slab, simulations are performed using a commercial simulation package CST Microwave Studio. The dimensions of loop antennas remain unchanged from the previous analysis, and the capacitors in both the matching network of the antenna and the CLSRR structures are implemented as lumped elements in simulations. In addition to the CLSRR structure, a dielectric slab is also placed between the CLSRR layers. The dielectric constant of the slab is varied in simulations to find the optimum enhancement of the WPT efficiency. It is found that when the dimensions of the CLSRR structures in Figure 11(a) are used, a dielectric constant of $\varepsilon=3.9$ provides the best results. Figure 12(b) shows the comparison of system efficiency for three WPT systems. It is clearly demonstrated that the efficiency enhancement by the CLSRR structure agrees well with that of the homogeneous IM slab, except for a slight frequency shift. Besides, the difference in the dielectric constant of the material is due to the difference in the effective permeability, according to Figure 6(b) that different combinations of μ_y and ε may provide similar enhancement of WPT efficiency.

5. CONCLUSION

In this article, we investigate the possibility of applying IMs for improving the efficiency of WPT systems. Through the analysis of transmission spectra for different metamaterial slabs, it is shown that when the slab thickness is small, which is essential for the practical system implementation, IM slabs outperform those formed by other types of metamaterials, such as MNG or DNG. This is due to the fact that a slab of IM introduces resonances that are located in close proximity and can be conveniently tuned to enable amplification of evanescent waves for a wide range of low-order wave numbers. It is demonstrated

that the location of the second resonance is sensitive to the slab thickness, relative permeability along the anisotropy axis, and the dielectric constant of the material.

Full-wave FDTD simulations of an IM-enhanced WPT system show that the system efficiency can be improved by an order of magnitude comparing with the conventional design, when the transverse dimension of the slab is large and the loss in the material is small. Results also show that at the frequency of 100 MHz, more than 60% of the transmitting power can be delivered to a distance of $\lambda/3$ when the thickness of the IM slab is only $\lambda/60$. As an example implementation of the IM slab, the CLSRR structure is considered and simulation results show good agreement with the homogeneous material. Future design of the IM slab may be focused on reducing material loss to further enhance the WPT efficiency.

REFERENCES

1. A. Marincic and D. Budimir, Tesla's contribution to radio wave propagation, Microwave Rev 7 (2001), 24–28.
2. W.C. Brown, Experimental airborne microwave supported platform descriptive note: Final Report., Jun 1964–Apr 1965.
3. A. Kurs, A. Karalis, R. Moffatt, J.D. Joannopoulos, P. Fisher, and M. Soljiacic, Wireless power transfer via strongly coupled magnetic resonances, Science 317 (2007), 83–86.
4. K.Y. Kim, Wireless power transfer: Principles and engineering explorations, Intech Open, 2012.
5. E. Nader and R.W. Ziolkowski, Metamaterials: Physics and engineering explorations, Wiley, Hoboken, NJ, 2006.
6. A. Grbic and G.V. Eleftheriades, Growing evanescent waves in negative-refractive-index transmission-line media, Appl Phys Lett 82 (2003), 1815.
7. T.J. Cui, X.Q. Lin, Q. Cheng, H.F. Ma, and X.M. Yang, Experiments on evanescent-wave amplification and transmission using metamaterial structures, Phys Rev B 73 (2006), 245119.
8. J. Choi and C. Seo, High-efficiency wireless energy transmission using magnetic resonance based on metamaterial, Prog Electromagn Res 106 (2010), 33–47.
9. B. Wang, K.H. Teo, T. Nishino, W. Yerazunis, J. Barnwell, and J. Zhang, Experiments on wireless power transfer with metamaterials, Appl Phys Lett 98 (2011), 254101.
10. Y. Urzhumov and D.R. Smith, Metamaterial-enhanced coupling between magnetic dipoles for efficient wireless power transfer, Phys Rev B 83 (2011), 205114.
11. D. Huang, Y. Urzhumov, D.R. Smith, K.H. Teo, and J. Zhang, Magnetic superlens-enhanced inductive coupling for wireless power transfer, J Appl Phys 111 (2012), 064902.
12. D.R. Smith and D. Schurig, Electromagnetic wave propagation in media with indefinite permittivity and permeability tensors, Phys Rev Lett 90 (2003), 0774051–0774054.
13. Y. Jin, Improving subwavelength resolution of multilayered structures containing negative-permittivity layers by flatting the transmission curves, Prog Electromagn Res 105 (2010), 347–364.
14. J.B. Pendry, Negative refraction makes a perfect lens, Phys Rev Lett 85 (2000), 3966–3969.
15. V.G. Veselago, The electrodynamics of substances with simultaneously negative values of ε and μ, Sov Phys Usp 10 (1968), 509–514.
16. A.I. Smolyakov, E. Fourkal, S.I. Krasheninnikov, and N. Sternberg, Resonant modes and resonant transmission in multi-layer structures, Prog Electromagn Res 107 (2010), 293–314.
17. R.M. Corless, G.H. Gonnet, D.E.G. Hare, D.J. Jeffrey, and D.E. Knuth, On the Lambert W function, Adv Comput Math 5 (1996), 329–359.

18. F.W. Grover, Inductance calculations: Working formulas and tables, Instrumentation Systems & Publication, Mineola, NY, 1982.

19. A. Taflove, Computational electrodynamics: The finite-difference time-domain method, 2nd ed., Artech House, Norwood, MA, 2000.

20. L. Rosenfeld, Theory of electrons, Dover Publications, New York, 1965.

21. Y. Zhao and Y. Hao, Full-wave parallel dispersive finite-difference time-domain modeling of three-dimensional electromagnetic cloaking structures, J Comput Phys 228 (2009), 7300–7312.

22. Y. Zhao, P.A. Belov, and Y. Hao, Accurate modelling of left-handed metamaterials using finite-difference time-domain method with spatial averaging at the boundaries, J Opt A Pure Appl Opt 9 (2007), 468–475.

23. J.P. Berenger, A perfectly matched layer for the absorption of electromagnetic waves, J Comput Phys 114 (1994), 185200.

24. M. Zargham and P.G. Gulak, Integrated CMOS wireless power transfer for neural implants, In: IEEE Biomedical Circuits and Systems Conference (BioCAS) (2011), 165–168.

25. D.R. Smith, W.J. Padilla, D.C. Vier, S.C. Nemat-Nasser, and S. Schultz, Composite medium with simultaneously negative permeability and permittivity, Phys Rev Lett 84 (2000), 4184–4187.

26. The American Radio Relay League, Small high efficiency loop sntennas for transmitting, The ARRL Antenna Handbook, 15th ed., 5–14, 1988.

27. C.L. Wagner and J.B. Schneider, Divergent fields, charge, and capacitance in FDTD simulations, IEEE Trans Microwave Theory Tech 46 (1998), 2131–2136.

28. D.R. Smith, S. Schultz, P. Markos, and C.M. Soukoulis, Determination of effective permittivity and permeability of metamaterials from reflection and transmission coefficients. Phys Rev B 65 (2002), 195104.

DESIGN OF WAVEFRONTS TRANSFORMERS WITH COMPLEMENTARY MEDIA

Yang Chen, Long Li, Cheng Zhu, Lei Lin, Ke Li, Feifei Huo, and Changhong Liang
National Key Laboratory of Antennas and Microwave Technology, Xidian University, Xi'an, Shaanxi 710071, People's Republic of China; Corresponding author: lilong@mail.xidian.edu.cn

ABSTRACT: *Since complementary media was proposed, it is widely used in electromagnetic cloaking. In this work, we realize some other optical devices that deal with wavefronts transformations with complementary media, which have obvious advantages over traditional ones. More importantly, we devise a novel-shape transformer that can create an illusion source to prevent the real source from being detected accurately. Some of these devices we develop can be realized with isotropic and homogenous materials. Influence of loss on optical performance is also explored. Moreover, the impact of evitable obstacles outside on the properties of these devices can be avoided by adding their complementary "images" inside these devices.* © 2014 Wiley Periodicals, Inc. Microwave Opt Technol Lett 56:875–879, 2014; View this article online at wileyonlinelibrary.com. DOI 10.1002/mop.28224

1. INTRODUCTION

In 2006, Pendry put forward the notion of manipulating electromagnetic (EM) wave via coordinate transformation [1]. Enormous applications from this idea were achieved, such as cloaks [1, 2], concentrators [3], rotators [4], EM bending devices [5], wave-shape transformers [6], anticloaks [7, 8], and so forth. Specifically, Ke et al. [9] proposed phase transformations between two arbitrary wavefronts based on transformation optics and ray optics where phase transformers with regular shapes were obtained.

Lai et al. [10] realized the complementary cloak based on the conception of complementary media and the complementary cloaks with various shapes and illusion cloaks were proposed soon afterward. Besides the applications of complementary media in cloaks, some more were brought forward via complementary media as well, such as super scatterers [11], super absorbers [12], waveguide devices [13], and so forth.

In this work, we deal with various transformations of wavefronts based on complementary media, including wavefronts translation and their variations in shape. Some corresponding devices, refractors, and shape transformers, are deigned, some of which can be realized via isotropic materials. And when there are evitable dielectric obstacles outside, we can obtain their complementary "images" through the according folding transformations, maintaining the good performance of these devices.

2. PRINCIPLES OF TRANSFORMATION

In this section, the folding transformations using complementary media for refractors, beam bends, the illusion devices for source, plane-to-cylindrical-wave transformers, and cylindrical-to-plane-wave transformers are detailed and shown in Figure 1. For each device, the transformation is to fold area S_2 (blue) into area S_1 (purple), and S_1 is the area that functions as a transformer. The wave propagates from left to right. The concrete transformations for these devices are detailed, respectively.

2.1. Refractors

For the translation of wavefronts, a refractor with complementary media is designed, as shown in Figure 1(a). Area S_2 is folded into its adjacent area S_1 with an angle deflection θ which is defined as refractive angle. And the folding transform can be written as

$$x' = k(x - a)$$
$$y' = y + x(k-1)\tan\theta + b(1-k)\tan\theta, \tag{1}$$

where $k = b/(b-a)$. According to Eq. (1), the permittivity and permeability in S_1 can be obtained [14]. Apparently, all the components of the derived constitute parameters are constants when θ is fixed, and after an easy calculation, they are written as

$$\bar{\bar{\varepsilon}}_{\text{refractor}} = \begin{bmatrix} k & (k-1)\tan(\theta) & 0 \\ (k-1)\tan(\theta) & [(k-1)^2\tan^2(\theta)+1]/k & 0 \\ 0 & 0 & 1/k \end{bmatrix}. \tag{2}$$

As is known widely, a rotated layered system can be utilized to mimic this refractor [15], and the fabulous properties of this refractor and its layered-system realization will be detailed in Section 3.

2.2. Shape Transformers

For the variations in the shape of wavefronts, we get beam bends, illusion devices for source, plane-to-cylindrical-wave transformers, and cylindrical-to-plane-wave transformers. Figures 1(b)–1(e) show their transformations, respectively. All the